Available online at www.sciencedirect.com
ScienceDirect
International Journal of Heat and Mass Transfer 51 (2008) 4025–4037
International Journal of HEAT and MASS TRANSFER
www.elsevier.com/locate/ijhmt

Minimizing hot spot temperature of porous stackings in natural convection

Charles Villemure, Louis Gosselin *, Guy Gendron

Département de génie mécanique, Université Laval, Québec City, Québec, Canada G1K 7P4

Received 18 April 2007; received in revised form 27 November 2007
Available online 17 March 2008

Abstract

Due to their large surface of heat transfer per volume, porous structures such as metallic foams are considered as an interesting alternative to fins. In this paper, we investigate the optimal configuration of a porous medium structure with the objective to minimize the hot spot temperature in natural convection. The heat sink is adjacent to a heat-generating plate, and consists of a stacking of porous layers, in which a cooling fluid circulates strictly driven by natural convection. The objective of this work is to minimize the hot spot temperature of the system. The design variables are the porosity and the material of each layer. The thermal performance is evaluated with a CFD code based on a finite volume approach. The hot spot temperature minimization is pursued with a genetic algorithm (GA) under global mass and cost constraints. The GA determines the optimal porosity and selects the most appropriate material of each layer. Furthermore, the optimal total length of the stacking is indirectly determined by the GA as layers can be added or removed in order to improve the global performance and/or satisfy the constraints. A mapping of the designs generated by the GA as a function of the mass and cost constraint combination reveals that an appropriate distribution of porosity and material benefits the overall thermal performance of the layered porous medium.

Keywords: Heat sink; Natural convection; Cooling; Genetic algorithms; Designed porous media

1. Introduction

In the last decades, the explosion of the communication and personal computer markets has forced fabricants to design electronic components that are constantly smaller and more powerful. Moreover, important efforts are dedicated to miniaturize such systems as exposed by the famous Moore's law [1]. For every advance in the performance of the devices, there is a correspondent increase in the heat that must be dissipated. In this context, thermal management has become fundamental in the design of efficient electronics systems [2]. In fact, the world market for thermal dissipaters was estimated at 4.4 billion $ in 2006 and is expected to grow to 6.7 billion $ by 2011 [3].

The cheapest and most reliable way to discharge heat to the surrounding environment is to rely on buoyancy-driven flows. For an air-to-surface temperature difference of 100 K, typical heat fluxes removed from electronics by self-driven flows vary between 0.05 and 0.1 W/cm^2 [4]. The current requirement for more compact thermal systems with larger heat transfer rate densities calls for the use of extended surfaces (e.g., fins) in natural convection (e.g., see [5]). A common feature that appears in the body of work published on the enhancement of buoyancy-driven heat transfer rate density is the emergence of a flow structures where solid heat-dissipating material and fluid streams are distributed optimally [6–8]. This observation led to the idea of "designed porous media" [9]. In recent years, many investigations [10–12] have been conducted to understand the role that could be played by metallic foams in thermal systems. The results are encouraging; by adjusting the pore diameter and porosity it is possible to greatly improve the

* Corresponding author. Tel.: +1 418 656 7829; fax: +1 418 656 7415.
E-mail address: Louis.Gosselin@gmc.ulaval.ca (L. Gosselin).

0017-9310/$ - see front matter © 2008 Elsevier Ltd. All rights reserved.
doi:10.1016/j.ijheatmasstransfer.2007.11.052

Nomenclature

c_p	specific heat, J kg^{-1} K^{-1}
D	pore diameter, m
f	objective function
g	gravitational acceleration, m s^{-2}
H	height, m
k	thermal conductivity, W m^{-1} K^{-1}
K	permeability, m^2
L	thickness of the heat sink, m
M	mass, kg
N	number of layers
P	pressure, N m^{-2}
q''	heat flux, W m^{-2}
Ra	Rayleigh number
T	temperature, K
u, v	velocity components, m s^{-1}
V	bulk velocity in a pore, m s^{-1}
x, y	Cartesian coordinates, m

Greek symbols

α	thermal diffusivity, m^2 s^{-1}
β	coefficient of thermal expansion, K^{-1}
ε	penalty coefficient
ϕ	porosity
μ	viscosity, N s^{-1} m^{-2}
ν	kinematic viscosity, m^2 s^{-1}
ρ	density, kg m^{-3}

Subscripts

f	fluid
co	constraint
eq	equivalent
max	maximal
opt	optimal
s	solid
w	wall
wco	without constraint

Superscript

$\sim$	dimensionless parameter

heat transfer rate density [13,14]. Different pore geometries have also been considered. For instance, a judicious positioning of micro-channels in a conductive matrix, resulting from a constructal approach, enhances heat transfer [15]. In a similar context, a heat exchanger composed of a juxtaposition of micro-channel has been optimized in Refs. [16–19]. In addition to cooling of electronics, several domains like geothermal systems, insulators, cooling towers, and catalytic reactors are important problems related to convection in porous media [20]. These studies show that an optimal network of pores emerges from the maximization of heat removal. The idea of using porous material to improve heat transfer in natural convection is investigated in [21]. A fibrous material is bonded to a surface in order to increase the fluid–solid interaction area. This approach reveals to be particularly efficient in terms of Nusselt number increase, especially for highly porous medium. Values as high as four times the average Nusselt number, without fiber coating, were predicted numerically.

In this paper, we minimize the hot spot temperature of a juxtaposition of porous layers used to cool down a heat-generating plate in natural convection. Mass, cost and dimension constraints are imposed. To achieve this result, a CFD code is coupled with a genetic algorithm (GA) toolbox. The result of the optimization is a stack of layers, each of which can be made of a different material and display a specific porosity.

2. Heat transfer and fluid flow modeling

Consider a stacking of porous layers attached to a heat-generating plate, Fig. 1. The stacking has a height H, and a total thickness L. An imposed uniform heat flux is applied to the left boundary and drives the fluid upward thanks to buoyancy. Heat leaves the heat sink from the top horizontal face and the right boundary is assumed adiabatic and impermeable. The temperature of the incoming fluid at the bottom surface is assumed to be T_∞. Although only four layers are shown in this figure, the heat sink can

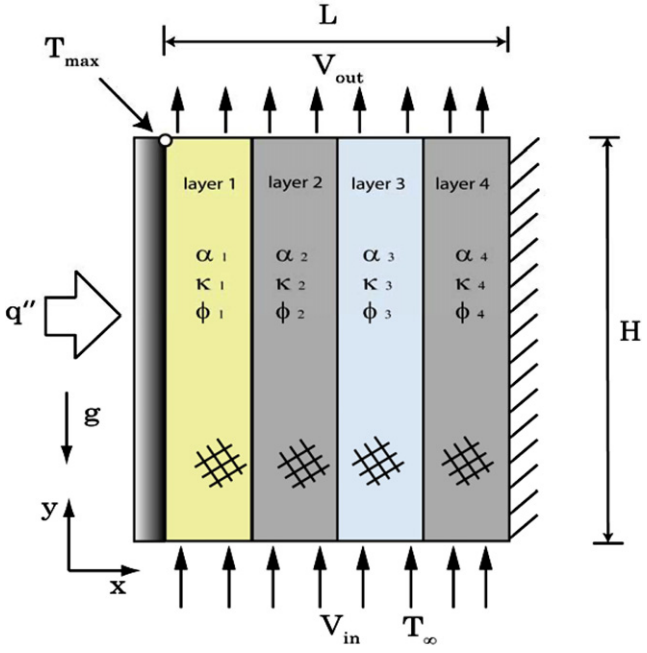

Fig. 1. Schematic representation of a stack of porous media layers used to cool a heat-generating plate in natural convection.

be made of any number of layers, N. In order to obtain an optimal design, the material of each layer can be selected from a library of available materials. It is also assumed that through appropriate processing, the porosity of the material can be adjusted to any value. It is worth to mention that the model considered needed sufficient simplicity for the optimization to be feasible, because during the optimization, several designs will be tested. For the fluid flow problem, we consider here that the porous media is made of a series of small pores aligned in the y-direction. This porous medium geometry results in a flow in the y-direction like in a chimney. The density of the pores in a layer determines the local porosity. Assuming Darcy flow, the y-direction velocity in the presence of gravity is

$$v = -\frac{K_y}{\mu}\left(\frac{\partial P}{\partial y} + \rho_f g(1-\beta[T-T_\infty])\right) \tag{1}$$

where the Boussinesq approximation has been invoked [22]. Note that with the porous structure considered here (i.e., pores aligned in the flow-direction), the breakdown of linearity engendered by the form drag due to solid obstacles [20] is negligible, and therefore, Darcy regime can be assumed for a much larger range of local Reynolds [23,24]. From mass conservation, we have $\partial v/\partial y = 0$. In other words, v is only a function of x. At a given location x, integrating Eq. (1) from $y = 0$ to $y = H$ yields

$$v(x) = \frac{g\rho_f \beta K_y}{\mu H}\int_0^H [T(x,y) - T_\infty]\mathrm{d}y \tag{2}$$

where the temperature profile $T(x,y)$ is unknown. To achieve Eq. (2) from Eq. (1), one sets $P(y=0) - P(y=H) = \rho_f$ gH as both ends of the channel are open to the ambient [22]. The determination of the temperature field is achieved with the conservation of energy equation. Assuming local thermal equilibrium as a first approximation and neglecting conduction in the direction of the flow, the energy balance can be written as [20,22]

$$v(x)\frac{\partial T}{\partial y} = \frac{\partial}{\partial x}\left(\alpha\frac{\partial T}{\partial x}\right) \tag{3}$$

where $\alpha = k_{\mathrm{eq,x}}/(\rho_f c_{p,f})$. The simplest strategy to estimate the equivalent thermal conductivity in the x-direction, $k_{\mathrm{eq,x}}$, and account for the presence of both the fluid and solid phases, would be to use the volume-averaged conductivity, $k_s(1-\phi) + k_f\phi$. However, this model does not take into account the anisotropy of the porous structure. In this paper, we use the result presented in [25] for a solid with cylindrical inclusions, and assume that the thermal conductivity of the liquid phase (i.e., inclusions) is much smaller than that of the solid, hence $k_f/k_s \ll 1$. Under these assumptions, the resulting x-direction conductivity is $k_s(1-\phi)/(1+\phi)$.

In this paper, we work with a dimensionless version of the governing equations, Eqs. (2) and (3):

$$\tilde{v}(\tilde{x}) = \widetilde{K} Ra \int_0^1 \widetilde{T}(\tilde{x},\tilde{y})\mathrm{d}\tilde{y} \tag{4}$$

$$\tilde{v}\frac{\partial \widetilde{T}}{\partial \tilde{y}} = \frac{\partial}{\partial \tilde{x}}\left(\tilde{k}\left(\frac{1-\phi}{1+\phi}\right)\frac{\partial \widetilde{T}}{\partial \tilde{x}}\right) \tag{5}$$

where the dimensionless variables and parameters are

$$\tilde{v} = \frac{v}{k_f/(\rho_f c_{p,f} H)}, \quad \widetilde{T} = \frac{T-T_\infty}{Hq''/k_f}, \quad \widetilde{K} = \frac{K}{H^2} \tag{6}$$

$$\tilde{k} = \frac{k_s}{k_f}, \quad Ra = \frac{\rho\beta H^4 q''}{k_f \alpha_f \mu} \tag{7}$$

Contrary to what is normally assumed, the Rayleigh number that we consider is not based on the permeability K because here, K will vary when the porosity is changed during the optimization. In a dimensionless form, the boundary conditions, are

$$\tilde{k}\left(\frac{1-\phi}{1+\phi}\right)\frac{\partial \widetilde{T}}{\partial \tilde{x}} = -1 \quad \text{at } \tilde{x} = 0 \tag{8}$$

$$\frac{\partial \widetilde{T}}{\partial \tilde{x}} = 0 \quad \text{at } \tilde{x} = L/H \tag{9}$$

$$\widetilde{T} = 0 \quad \text{at } \tilde{y} = 0 \tag{10}$$

$$\frac{\partial \widetilde{T}}{\partial \tilde{y}} = 0 \quad \text{at } \tilde{y} = 1 \tag{11}$$

It is well known that the porosity and permeability are related to one another. Considering the porous media geometry described above (i.e., pores aligned in the y-direction), the permeability–porosity relation is [23,24]

$$\widetilde{K}(\phi) = \frac{1}{32}\phi\left(\frac{D}{H}\right)^2 \tag{12}$$

In this paper, the diameter of the pores, D, is considered as a known parameter (non-designable). Larger values of D result in larger permeabilities which is beneficial. However, the present model would fail for too large values of D as local thermal equilibrium could not be assumed anymore.

During the optimization, mass and cost will be constrained. The total mass of the system is the summation of the mass of each layer

$$\widetilde{M} = \frac{M}{\rho_f H^2} = \sum_{j=1}^{N} \tilde{\rho}_j(1-\phi_j)\Delta\tilde{x}_j \tag{13}$$

where N is the number of layers considered and $\Delta\tilde{x}_j$ is the thickness of the jth layer. Similarly, it is also possible to consider a total relative cost constraint, which is the summation of the relative cost associated with each layer, i.e.,

$$\widetilde{C} = \sum_{j=1}^{N} \tilde{\rho}_j \tilde{c}_j(1-\phi_j)\Delta\tilde{x}_j \tag{14}$$

The general problem can be formulated as follows:

$$\begin{aligned} \text{Minimize}: \quad & \widetilde{T}_{\max} = \max(\widetilde{T}(\tilde{x},\tilde{y})) \\ \text{Varying}: \quad & \phi_j, \text{material}_j \text{ with } j = 1, N \\ \text{While respecting}: \quad & r_{\mathrm{m}} \geqslant \widetilde{M}/\widetilde{M}_{\mathrm{wco}} \\ & r_{\mathrm{c}} \geqslant \widetilde{C}/\widetilde{C}_{\mathrm{wco}} \end{aligned}$$

where r_{m} and r_{c} represent respectively mass and cost ratio of the value obtained in an optimization conducted without constraint (wco) for the correspondent parameters $Ra\widetilde{D}^2$, $\widetilde{L}$ and N. A constraint is considered respected if the value of the ratios r_{m} and r_{c} are smaller than the limitation imposed ($\widetilde{M}/\widetilde{M}_{\mathrm{wco}}$ and $\widetilde{C}/\widetilde{C}_{\mathrm{wco}}$). A database of the potential material candidates with their corresponding properties is presented in Table 1. Designs in the coming sections of this paper might include empty layers. This happens when the porosity reaches 1 in a layer, making the downward layers totally inefficient at dissipating heat. Those will be denoted "*V*" and assumed to have no conductivity or mass. Empty layers will also be assumed to have no associated cost.

Before ending this section, it is worth to mention a few words about the local thermal equilibrium (LTE) assumption. Several authors have studied whether LTE is valid or not for different geometries and conditions (e.g., pore diameters, flow conditions, solid-to-thermal conductivity ratio) (e.g., [24,26,27]). Kim et al. [26] proposed useful figures to determine the applicability of a one-temperature model. Translated in terms of our notations, the error induced with a one-temperature model could be expressed as a function of $\widetilde{K}$ and $\phi[\tilde{k}(1-\phi)]^{-1}$. In our case, we have $\phi[\tilde{k}(1-\phi)]^{-1} \sim \mathrm{O}(10^{-2}-10^{-3})$. Allowing a 10% error thus means according to [26] that $\widetilde{K}$ should be smaller than $\mathrm{O}(10^{-3}$–$10^{-4})$. The error introduced by the LTE-assumption was thus considered acceptable, and future work could relax the LTE-assumption by introducing a two-temperature model. Furthermore, the simplicity provided by the one-temperature model was convenient to perform the optimization in a feasible CPU time, as several designs will be tested during the optimization process. In any case, Leblond and Gosselin [24] showed that even though the use of a one-equation model can lead to a different level of performance than that achieved with a two-temperature model (i.e., different $T_{\max}$-values), the architectures of optimized heat sink designs achieved with both models are similar for mass-constrained problems.

Table 1
Properties of aluminum, copper and iron normalized with that of air evaluated at 300 K [28], and relative cost per unit of mass normalized with the cost of iron [29]

j	Material	Density, $\tilde{\rho}$	Conductivity, $\tilde{k}$	Relative cost, $\tilde{c}$
1	Aluminum (Al)	2327.5	9011.4	6
2	Copper (Cu)	7691.6	15247.2	12
3	Iron (Ir)	6776.3	3049.4	1

3. Heat transfer and fluid flow calculations

A code based on the finite volume approach [30] has been used to solve Eqs. (4) and (5) and obtain the temperature and velocity fields. The domain of Fig. 1 is discretized with a structured mesh with N_y quadrilateral cells per unit of length in both directions and Eq. (5) is integrated on each control volume. An upwind scheme is applied to the convective term of Eq. (5), and a centered second-order scheme is used for the diffusive term. The conductivity at the face of the control volume is extrapolated with harmonic means [31]. The resulting set of linear algebraic equations is solved line-by-line with a tridiagonal solver. The sweeping is performed in the direction of the flow. The calculation of the velocity profile does not require the solution of a differential equation, and is straightforward from Eq. (4).

Eqs. (4) and (5) are coupled: $\tilde{v}$ is required to determine $\widetilde{T}$, and vice versa. Therefore, an iterative procedure has to be implemented. First, a velocity profile is assumed, then the temperature profile is calculated by solving Eq. (5) with the code described above. The temperature profile that is obtained is used to update the velocity profile, Eq. (4). The procedure is repeated until convergence. Convergence is reached when the change in the normalized norm of both the velocity and temperature profiles, between two consecutive iterations, is smaller than 0.1%

$$\frac{1}{\zeta_{T,\mathrm{mean}}}\sqrt{\int_0^1\int_0^{\widetilde{L}}(\widetilde{T}_{it}(\tilde{x},\tilde{y})-\widetilde{T}_{it-1}(\tilde{x},\tilde{y}))^2\,\mathrm{d}\tilde{x}\,\mathrm{d}\tilde{y}} < 10^{-3} \quad (15)$$

$$\frac{1}{\zeta_{v,\mathrm{mean}}}\sqrt{\int_0^{\widetilde{L}}(\tilde{v}_{it}(\tilde{x})-\tilde{v}_{it-1}(\tilde{x}))^2\,\mathrm{d}\tilde{x}} < 10^{-3} \quad (16)$$

where $\zeta_{v,\ \mathrm{mean}}$ and $\zeta_{T,\ \mathrm{mean}}$ are, respectively, the Euclidian norm of the velocity and temperature variations over the five first iterations. Use of more stringent convergence criteria than Eqs. (15) and (16) resulted in negligible changes in the results. Typically, ~15 sweeps for the resolution of the temperature and velocity profiles were required to satisfy both convergence criteria. This means that for calculating the hot spot temperature for a given set of design parameters (i.e., porosities, materials), one is required to solve $15N_y\widetilde{L}$ tridiagonal systems of dimensions $N_y\widetilde{L} \times N_y\widetilde{L}$.

An example of a mesh independence study is given in Table 2. A low number of cells (N_y) per unit length is initially chosen and the hot spot temperature is calculated. Then, N_y is doubled until further mesh refinement leads to relative difference on hot spot temperature smaller than 1%. We found that the mesh density required varies with the parameter $Ra\widetilde{D}^2$ and with the porosity, as revealed in Table 2. For a given parameter $Ra\widetilde{D}^2$, the requires value of N_y increased with ϕ. In addition, structures fabricated with multiple layers composed of different materials and porosities, similar to the ones that are optimized in the present work, have been studied. The results show that the anisotropic distribution of porous material in the heat exchanger model considered has much less impact on the

Table 2
Mesh independence study for a single layer aluminum heat sink with $\widetilde{L} = 0.5$, $\phi = 0.95$, $N = 1$ (without constraints)

i	N_y	$Ra\widetilde{D}^2 = 10^8$		$Ra\widetilde{D}^2 = 10^{12}$	
		$\widetilde{T}_{\max}$	$\left\lvert\frac{\widetilde{T}_{\max,i}-\widetilde{T}_{\max,i+1}}{\widetilde{T}_{\max,i+1}}\right\rvert$	$\widetilde{T}_{\max}$	$\left\lvert\frac{\widetilde{T}_{\max,i}-\widetilde{T}_{\max,i+1}}{\widetilde{T}_{\max,i+1}}\right\rvert$
1	15	1.743×10^{-3}	–	4.657×10^{-5}	–
2	30	1.745×10^{-3}	1.66%	6.148×10^{-5}	32.2%
3	60	1.746×10^{-3}	*0.01%*	6.881×10^{-5}	11.91%
4	120	–	–	7.598×10^{-5}	10.43%
5	240	–	–	7.825×10^{-5}	2.98%
6	480	–	–	7.884×10^{-5}	*0.75%*

mesh density requirement than the porosity. Therefore, in our simulations, we used the mesh density dictated by large ϕ-values. For $Ra\widetilde{D}^2 = 10^8, 10^9, 10^{10}, 10^{11}$, and 10^{12}, the required values of N_y for mesh independence are respectively 30, 60, 120, 240, and 480.

4. Validation of the "CFD" code

In this section, the code is validated in the "thermal boundary layer" regime (for which an analytical solution could be found). This means that the heat sink studied in this validation section is large enough so that the fluid leaving the exit plane at the right-hand side of the system showed in Fig. 1 has not felt the presence of the warm plate (i.e., $\widetilde{T}(\widetilde{L}, 1) \leqslant 1\%\widetilde{T}_{\max}$). For instance, at $Ra\widetilde{D}^2 = 10^8$, the required system length to achieve the boundary layer regime is $\widetilde{L} = 10$. Moreover, the heat sink is composed of a single layer made of copper. We do not expect the optimized heat sink to operate in that regime. However, an analytical solution could be found in that limit, so we used it to valid our code.

An analytical solution based on integral method [32] has been developed to determining the hot spot temperature in the thermal boundary layer regime:

$$\widetilde{T}_{\max} = 1.65\left(\frac{1}{Ra\tilde{k}_{\mathrm{eq}}\widetilde{K}}\right)^{1/3} \tag{17}$$

This solution is valid uniquely for single layer heat sink operating in the thermal boundary layer limit. Our CFD code agreed with Eq. (17) within 10%. Considering the fact that Eq. (17) is valid from an order of magnitude point view, the agreement has been judged satisfactory. It is interesting to note that when replacing Ra, $\tilde{k}_{\mathrm{eq}}$, and $\widetilde{K}$ by their definitions, Eqs. (6), (7) and (12), $\widetilde{T}_{\max}$ as given by Eq. (17) is minimal when $\phi_{\mathrm{opt}} = 0.41$. This result will be illustrated later.

Moreover, we validated our CFD code with a commercial thermofluid software [34]. A heat sink identical to that presented in Section 3 has been modeled with this software. The agreement was very good. The difference between the values of $\widetilde{T}_{\max}$ calculated by the commercial code and the values obtained from our CFD code are within 1%. This agreement has been verified for $Ra\widetilde{D}^2$ numbers varying between 10^8 and 10^{11} and porosity values ranging from 0 to 0.95. In our "CFD" code $\phi = 1$ designates a void layer which acts as an adiabatic boundary. For this reason, the validation with a single layer heat sink has been conducted at a highest porosity of 0.95.

5. Optimization procedure with genetic algorithms (GA)

As mentioned above, our objective is to minimize the hot spot temperature of the system of Fig. 1 in natural convection under global mass and cost constraints. A genetic algorithm (GA) toolbox [35] has been used to achieve that goal. The design parameters are the porosities and solid material of each layer. A design is represented by a set of two chromosomes: one chromosome for the materials and one for the porosities. Each chromosome contains N genes where N is the number of layers, each gene representing a design variable. The N first genes define the material of each layer. An integer, which varies between 1 and 4, identifies the material of the layer (see Table 1). Therefore two bits are required to characterize a material. The fourth possibility is reserved for an empty layer. The second set of N variables contains genes corresponding to the porosity of each layer. We chose to represent the porosity with a set of 5 bits, which leads to a precision in terms of porosity of $1/(2^5) = 3 \times 10^{-2}$. A design (individual) is the concatenation of the porosity chromosome ($5N$ bits), and materials chromosome ($2N$ bits), and thus has $7N$ bits.

The optimization procedure is summarized in Fig. 2. Only the main steps are presented here, the detailed procedure being available in [32]. An initial population of 25 designs is generated randomly in binary form. Gray code is employed as the binary numeral system, as this representation tends to accelerate the convergence of a search performed with continuous variables [36].

After the bit sequences have been decoded, each specific configuration (design) is known. As a result of the random process used to create the initial population, the heat sink architecture might not respect physical requirements. For example, a heat sink with an empty layer that is not positioned at the very end of its structure represents a physical aberration. Also, a correction is applied to ensure a coupling between the material and porosity variables of a layer. An empty layer ($\phi = 1$) must be designated by the symbol related to a void space (V) and not by a symbol referring to one of the possible materials.

The next step consists in evaluating the performance of each individual. This step requires solving the thermofluid problem associated to a phenotype by using the CFD code described in Section 3. The objective function f corresponds to the hot spot temperature $\widetilde{T}_{\max}$, penalized to take into account the mass and cost constraints:

$$f = \widetilde{T}_{\max}\left(\varepsilon_{\mathrm{m}}\left(\mathrm{Max}\left[\frac{\widetilde{M}}{\widetilde{M}_{\mathrm{co}}} - 1, 0\right]\right)^2 + 1\right) \times \left(\varepsilon_{\mathrm{c}}\left(\mathrm{Max}\left[\frac{\widetilde{C}}{\widetilde{C}_{\mathrm{co}}} - 1, 0\right]\right)^2 + 1\right) \tag{18}$$

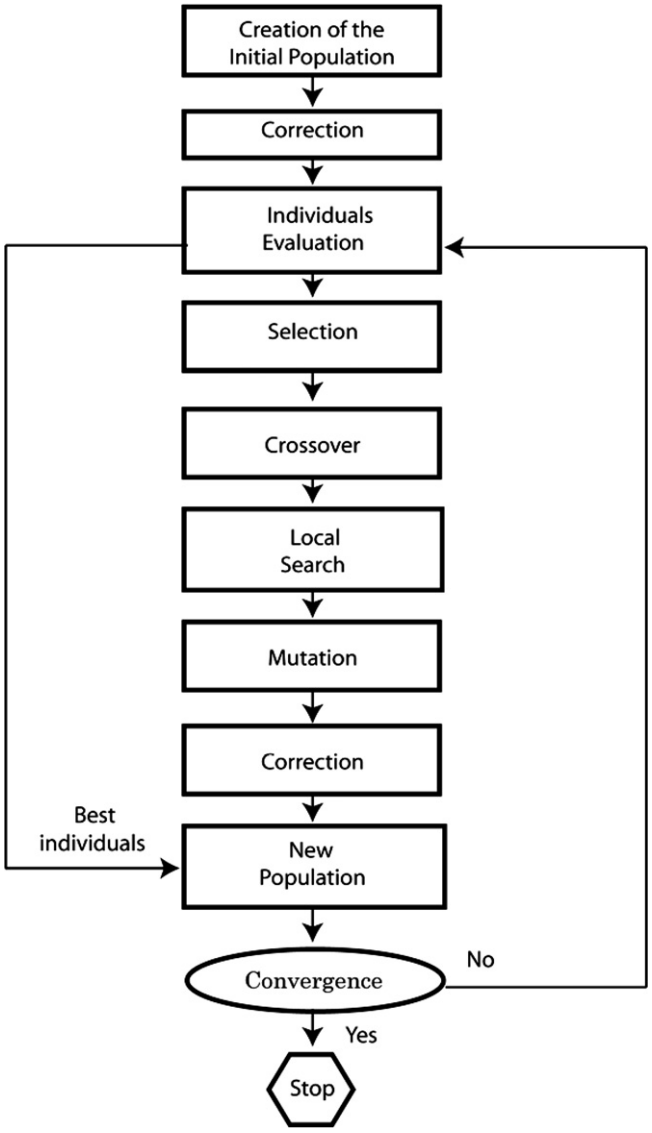

Fig. 2. Main steps of the optimization procedure with a genetic algorithm.

The mass and cost limits are respectively denoted $\widetilde{M}_{co}$ and $\widetilde{C}_{co}$. With Eq. (18), a design that does not respect either constraint (i.e. $\widetilde{M}/\widetilde{M}_{co} > 1$ or $\widetilde{C}/\widetilde{C}_{co} > 1$) will see its objective function penalized. The parameters ε_m and ε_c impair the performance function when the constraints are violated. Typically the parameters ε_m and ε_c are set to 10. When the constraints are respected, the objective function becomes simply the hot spot temperature $\widetilde{T}_{max}$.

The "parents" are then selected based on their fitness: designs with smaller values of f have better chances of being selected as parents. The technique utilized in this work to select individuals for recombination is a stochastic universal sampling (SUS). Parents are then crossed to create children. The crossing is done by randomly selecting a bit position in the sequence of bits that characterizes the designs (crossing point), and combining the bit sequence that precedes the crossing point of one individual with the bit sequence following the crossing point of the other parent.

In order to facilitate the exploration of the domain, a local search is coupled to the genetic algorithm. The "neighbourhood" of an individual consists of designs that are very similar to the one investigated and present a slight variation in the set of design variables. For instance, one neighbour may have the same material sequence, with a slightly larger of smaller porosity value in one layer. The local search allows to consider solutions that might be difficult to generate otherwise only by mutation and crossover. Mutations (bit flipping) are then randomly applied to the offspring. The performances of the offsprings are evaluated and the new generation of designs is generated. To construct the new generation, an elitist procedure is chosen. The five best designs found in the previous generation are ensured to propagate in the new generation. Then, twenty individuals among the children are selected randomly, with larger probability for the fittest. Generation increments are continued until "convergence". The convergence criterion is set to 250 consecutive generations without improvement of the best design.

6. Hot spot temperature minimization without constraints

In this section, we begin by optimizing the porosity and material distributions without constraints. The objective function, Eq. (18), is then simplified to $f = \widetilde{T}_{max}$. Therefore, the best design corresponds to the one with the lowest hot spot temperature, regardless of its mass or cost. The optimization with a GA is a stochastic process. Consequently, different calculations performed with identical parameters might not require the same number of generations to reach the convergence criterion, and might not converge to the same design. In order to verify the repeatability offered by the GA, each simulation was performed ten times for each case studied here and the best design among the 10 runs is presented. The structure that we consider is made of 10 layers ($N = 10$).

In a non-constrained environment, every design that we obtained is made of copper only, the second material listed in Table 1. Even though copper is the heaviest and the most expensive of all, this choice is inevitable because it has the best thermal properties among the available constituents. Moreover, the repeatability of results is excellent.

First, let us examine the porosity distribution assigned by the GA as a function of the Rayleigh number, Fig. 3. We observed that the porosity increases gradually from the warm wall to the adiabatic frontier. This design is analogous to the one reported in [37] which investigated the optimal fin shape in natural convection. The geometry proposed by [37] possesses a large base and its width gets thinner toward the tip. Similarly, the optimal designed porous media obtained in this study presents less room dedicated to fluid near the heat source than at the opposite wall. Furthermore, in the simulations performed with low *Ra*, the GA converged to structures denser than those obtained with high Rayleigh numbers. These results indicate that the larger buoyancy forces associated with large *Ra* values

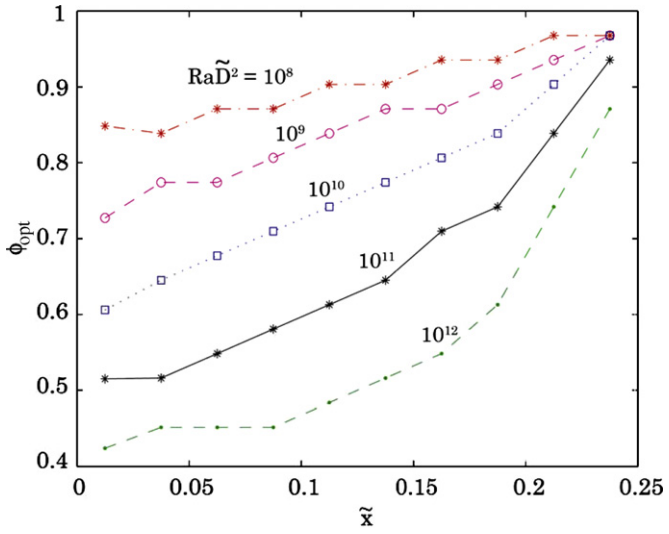

Fig. 3. Optimal porosity distribution in an unconstrained heat sink ($\widetilde{L} = 0.25$, $N = 10$, $\varepsilon_m = 0$ and $\varepsilon_c = 0$).

result in more fluid (higher porosity) being required to maintain a lower $\widetilde{T}_{max}$. The investigation also reveals that in the thermal boundary layer regime (e.g., see the curve for $Ra\widetilde{D}^2 = 10^{12}$, Fig. 3), the porosity close to the warm plate levels off around the optimal value of 0.41 predicted by the analytical approach employed to determine Eq. (17).

Next, we consider the impact of the heat sink length on the thermal performance. A series of optimizations performed with the GA were conducted for different values of $\widetilde{L}$ without mass and cost constraints. In Fig. 4 is shown the minimized hot spot temperature $\widetilde{T}_{max}$ as a function of the system length for different Rayleigh number. Each mark on the graph corresponds to the best design among the 10 runs performed with the same parameters. For a given *Ra*, hot spot magnitude decreases with an increasing

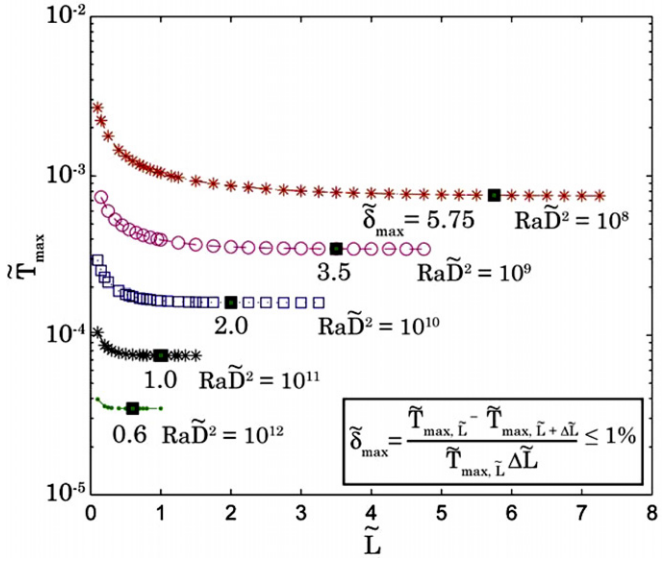

Fig. 4. Minimized hot spot temperature $\widetilde{T}_{max}$ as a function of $\widetilde{L}$ and $Ra\widetilde{D}^2$ for an unconstrained heat sink ($N = 10$, $\varepsilon_m = 0$ and $\varepsilon_c = 0$).

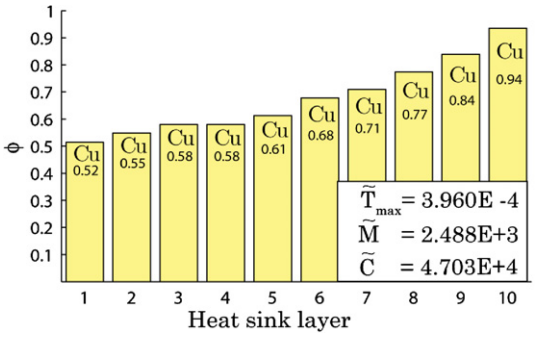

Fig. 5. Optimal unconstrained design for $Ra\widetilde{D}^2 = 10^9$, $\widetilde{L} = 1$ and $N = 10$.

$\widetilde{L}$. We notice that beyond a certain point, the maximal temperature levels off and no improvement is obtained beyond a certain length (diminishing return). The length at which the plateau appears scales as the boundary layer thickness at the heat sink outlet, i.e. $\widetilde{L} \approx \tilde{\delta}_T(\tilde{y} = 1)$. The numerical values of these $\widetilde{L}$ values are 5.75, 3.5, 2.0, 1.0 and 0.6 for $Ra\widetilde{D}^2$ of 10^8, 10^9, 10^{10}, $10^{11}$and 10^{12}, respectively.

In Fig. 5, we present the details of the optimal design found with $Ra\widetilde{D}^2 = 10^9$ and with $\widetilde{L} = 1$. This solution will serve as a reference in the rest of the paper to measure the performance of other designs obtained in a constrained environment. We chose that value of $Ra\widetilde{D}^2$ because it offered a good trade-off between conduction and convection as heat removal mechanisms. The ideas developed in this paper could be easily extended to other $Ra\widetilde{D}^2$-values. To achieve the porous architecture presented in Fig. 5, the GA required between 425 and 707 generations to converge.

7. Optimization under mass constraint

After the analysis of unconstrained optimal designs, we consider the influence of a mass limitation on the optimal design of the heat sink. The values of the critical mass $\widetilde{M}_{co}$ are determined in relation with the results obtained in the unconstrained case. Therefore, the mass constraint corresponds to a fraction of the optimal weight found for specific $\widetilde{L}$ and $Ra\widetilde{D}^2$-values for the unconstrained problem. As in the previous section, we consider a 10-layer heat sink built with the four materials listed in Table 1. It is recalled that the resulting unconstrained design achieved by the GA for $Ra\widetilde{D}^2 = 10^9$ and $\widetilde{L} = 1$ was presented in Fig. 5. The design in this figure will serve as a reference to measure the impact of the mass limitation on the optimal heat sink architecture. We thus consider mass constraints corresponding to 75%, 50%, 25% and 10% of the mass shown in Fig. 5. The designs generated by the GA are illustrated in Fig. 6.

At first, we realize that the mass constraint is respected in every case. In addition, the weights of the optimal structures correspond to the critical mass imposed. Hence, in the design domain, the optimal solutions are located at the constraint boundary. In the different simulations presented

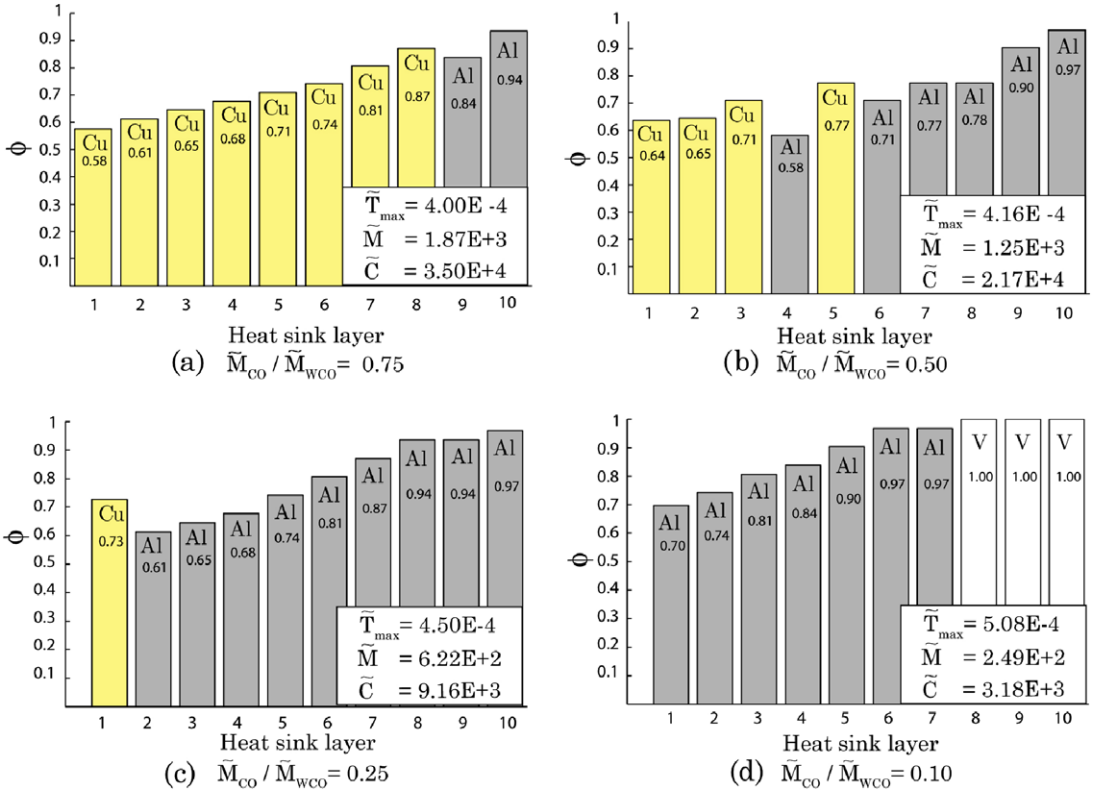

Fig. 6. Optimal designs with a progressively more stringent mass constraint for $Ra\tilde{D}^2 = 10^9$, $\tilde{L} = 1$, $N = 10$ and $\varepsilon_c = 0$.

in Fig. 6 the GA employs three mechanisms to minimize the mass of the structure: material substitution, porosity increase and layer elimination.

For constraints of $\tilde{M}_{CO}/\tilde{M}_{SCO} = [0.75, 0.50]$ (see Fig. 6a and b), we observe that copper, preferred material in the non-constrained problem, is replaced by aluminum. This substitution yields mass reduction without impairing to much the heat sink thermal performance. The aluminum portion is located in the very last layers in such a way that the layers positioned close to the heat source remain in copper. The portion of the heat sink close to the warm wall is pierced by the most intense heat currents. Consequently, the first layers have a great importance in terms of heat transfer. It is then essential to select a material with a conductivity as high as possible in the portion adjacent to the heat-generating wall. The combination Al–Cu offers a good trade-off between weight and thermal performances of the structure. In fact, this combination could be found on the heat sink market for electronic cooling (e.g., [33]).

When the mass constraint becomes more stringent, aluminum is used in a larger portion of the structure. In Fig. 6c, copper is completely eliminated except in the first layer that still remains in copper. We also observed that the porosity of the exchanger is increased to reduce its weight. The distribution of porosity evolves similarly to that in a non-constrained situation. The layers get denser toward the heat source. However, too large a porosity value impairs the equivalent conductivity expressed as $k_{eq} = k_s(1-\phi)/(1+\phi)$ and as a result, alters the thermal resistance of the system. To achieve better thermal performance within the mass limitation, the GA eventually chooses to eliminate layers. This mechanism creates room to assign more material in the most efficient region. The sacrificed layers are located at the end of the structure where heat current is less intense. By this process, the GA indirectly adjusts (i.e., optimize, design) the length of the heat sink.

Inevitably, the modifications imposed by the GA on the heat sink to satisfy the mass constraint deteriorate thermal performances. The hot spot temperatures achieved in Fig. 6a-d are respectively 1%, 5%, 13.6% and 28.3% higher than those obtained without constraint.

In order to better understand the influence of mass constraint on the heat sink architecture, multiple optimizations under gradually more stringent mass constraint have been conducted. The results of this investigation are summarized in Fig. 8. The curve marked with blue squares corresponds to optimizations performed solely under mass constraint (i.e., with $\varepsilon_c = 0$). This curve reports the cost of the designs achieved under different mass constraints. This curve indicates a nearly linear relationship between the optimal weight and the cost of the corresponding design. This observation will be discussed later in details in Section 9.

8. Optimization under cost constraint

Similarly to the procedure described in the previous section, the hot spot temperature of a 10-layer heat sink has

been minimized this time under a cost limitation. The reference structure corresponds to the unconstrained configuration presented earlier in Fig. 5. Four optimizations are conducted with constraints $\widetilde{C}_{co}/\widetilde{C}_{wco}$ equal to $[0.75, 0.5, 0.25, 0.1]$ and $\varepsilon_m = 0$. The results are presented in Fig. 7.

We observe that the same three mechanisms, presented in Section 7 are used to reduce the heat sink cost. For a moderate cost constraint, the GA substitutes the material of less effective layers by cheaper constituents, in this case aluminum and iron. For example, the layers near the heat source are replaced by aluminum and the ones situated at

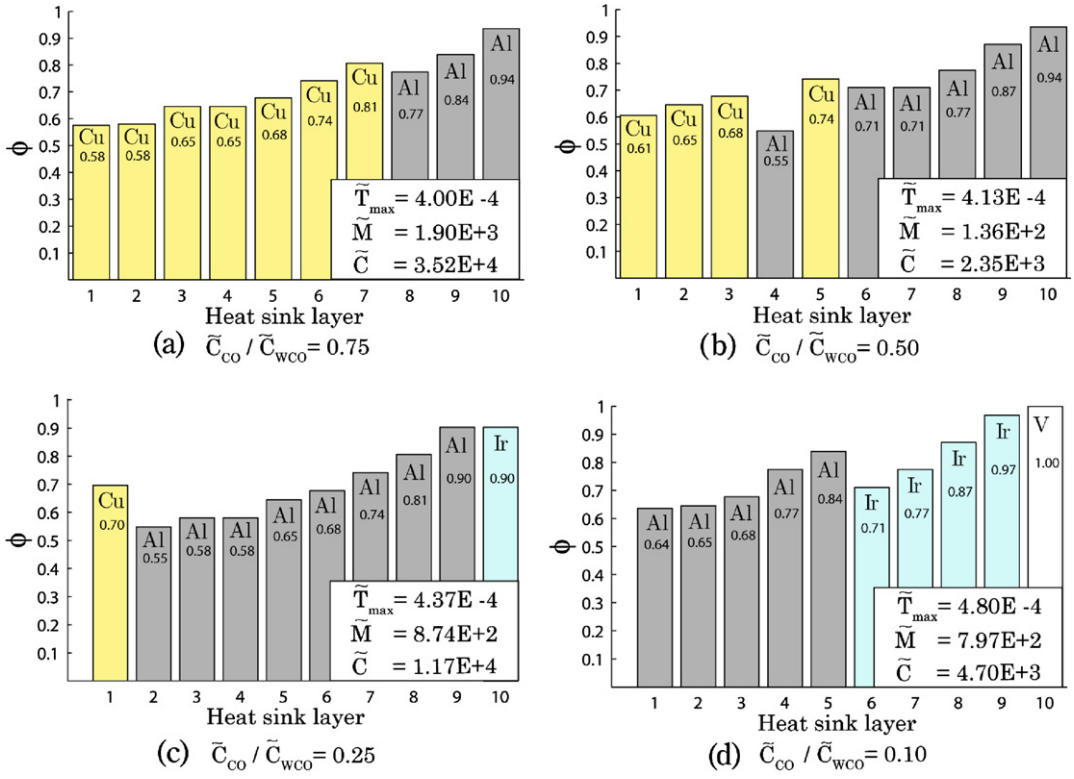

Fig. 7. Optimal designs with a progressively more stringent cost constraint for $Ra\widetilde{D}^2 = 10^9$, $\widetilde{L} = 1$, $N = 10$ and $\varepsilon_c = 0$.

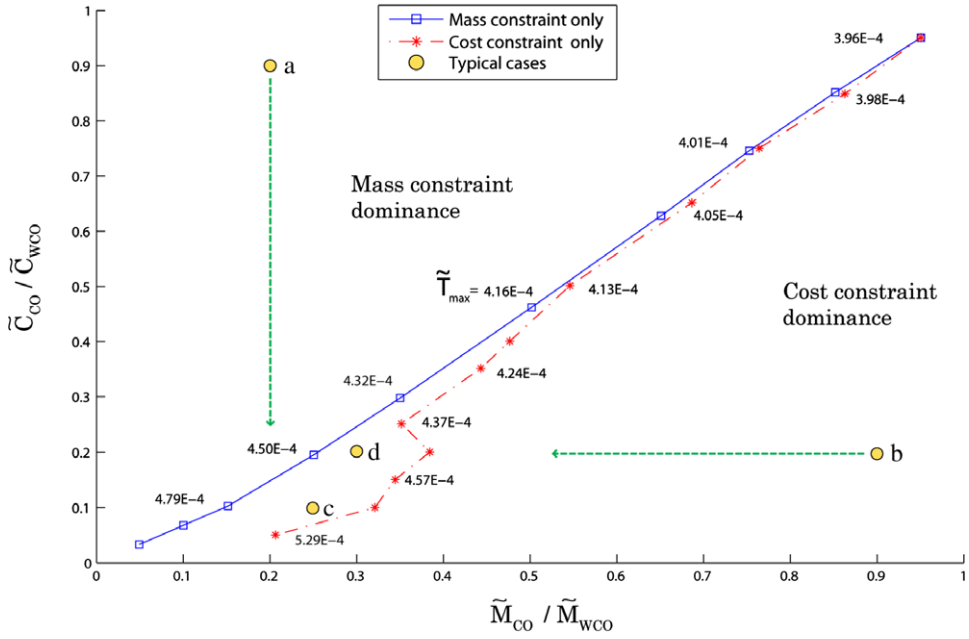

Fig. 8. Constraint space for $Ra\widetilde{D}^2 = 10^9$, $\widetilde{L} = 1, N = 10$ and $\varepsilon_c = 0$.

the end of the structure are progressively replaced by iron. Although this material has poor thermal properties compared to aluminum or copper, it represents the least expensive alternative. This process allows the GA to maintain the first layer in copper. Also, the global density of the structure is lowered in order to reduce the amount of material needed and indirectly the cost. For a very low value of $\widetilde{C}_{co}/\widetilde{C}_{wco}$ (see Fig. 7d), we see that an adequate thermal performance can no longer be achieved by adjusting porosity and material distribution only. Part of the cooling system must be removed to reallocate the corresponding cost reductions to the layers adjacent to the heat source. This is when empty layers appear at the right of the heat sink. These geometrical modifications influence the maximal temperatures in the resulting systems. As we decrease the value of $\widetilde{C}_{co}/\widetilde{C}_{wco}$ from 0.75 to 0.1, corresponding increases of $\widetilde{T}_{max}$ between 1% and 21.2% are obtained.

Similarly to the approach used with mass constraint, the impact of a gradually more stringent cost constraint is investigated by a series of optimization conducted under various ratio of $\widetilde{C}_{co}/\widetilde{C}_{wco}$. The results of this investigation are summarized in Fig. 8 by a red[1] star curve indicating the optimal mass corresponding to the cost imposed. The discussion of this curve follows in the next section.

9. Optimization under a combination of mass and cost constraints

In this section, we study the influence of a combination of mass and cost constraints on the heat sink architecture. In order to effectively measure the influences of a double constraint, we optimize a 10 layer structure with $\widetilde{L} = 1$ and operating at $Ra\widetilde{D}^2 = 10^9$ as presented above.

In order to better understand the interaction between the mass and cost constraints, optimizations with both constraints simultaneously applied have been conducted for different combinations of $\widetilde{M}_{CO}/\widetilde{M}_{WCO}$ and $\widetilde{C}_{CO}/\widetilde{C}_{WCO}$. The results of this investigation are summarized in Fig. 8. As mentioned above, the curve marked with blue squares corresponds to optimizations performed solely under mass constraint (i.e., with $\varepsilon_c = 0$), indicating a nearly linear relationship between the optimal weight and the cost of the corresponding design. The second curve, plotted in red, results from optimizations performed under a cost constraint only. For cost constraints such that $\widetilde{C}_{CO}/\widetilde{C}_{WCO} > 0.5$, the mass of the optimal heat sink varies proportionally to its cost. In this region of Fig. 8, the two curves merge. This means that the same design will be obtained when either constraint is applied separately. In other words, if a specific mass limitation is imposed (located in the region where $\widetilde{M}_{CO}/\widetilde{M}_{SCO} > 0.5$), an associate cost is obtained. If this cost is used as a limitation rather than the mass constraint, the same optimal design is found.

When either of the cost or mass constraint becomes more stringent, differences appear between the optimal designs obtained with each constraint. This behavior is explained by the introduction of iron in the optimal design. When the emphasis is placed on cost saving, iron then becomes a valid alternative. As predicted, the thermal performances of solutions emerging from severe constraints (limited design domain) are diminished. To quantify this behavior, the hot spot temperatures of the designs located on the mass and cost constraint curves are reported in Fig. 8.

Overall, Fig. 8 reveals three distinct regions. We observe that optimizations conducted with a combination of constraints ($\widetilde{M}_{CO}/\widetilde{M}_{SCO}$ and $\widetilde{C}_{CO}/\widetilde{C}_{SCO}$) that corresponds to a point located above the mass constraint curve (blue) results in a design dominated by the mass limitation. In other words, in that region, only the mass constraint can be active. For example, if $\widetilde{C}_{CO}/\widetilde{C}_{SCO}$ is set to 0.9 and $\widetilde{M}_{CO}/\widetilde{M}_{SCO}$ to 0.2 (point 1 in Fig. 8), the resulting cost will be 0.16, much less than the imposed upper limit of 0.9. Similarly, optimizations located below the cost constraint curve (red), are dominated by cost limitation. For example, for point 2 in Fig. 8 ($\widetilde{M}_{CO}/\widetilde{M}_{SCO} = 0.9$ and $\widetilde{C}_{CO}/\widetilde{C}_{SCO} = 0.2$), the mass of the design depends on the cost limitation which is the most stringent criterion. In this case, only the cost constraint is active. In the region bounded by the two curves, the two constraints are active (e.g., points 3 and 4). In Fig. 9, simulations conducted in the three specific zones of Fig. 8 are presented. The designs features corresponding to points 1 to 4 in Fig. 8 are shown in Fig. 9. Optimizations 3 and 4 present designs obtained with a combination of active constraints. As a matter of fact, in these simulations both the mass and the cost constraints are active.

From a global perspective, we have seen that the material sequence in the heat sink structures depends on where a set of constraints is located in the constraint domain (Fig. 8). In order to perceive general trends in the optimal heat sink composition, we constructed Fig. 10 which represents the "concentration" of a specific material in the final design according to the pair of constraints. Similarly to Fig. 8, the most stringent limitations are located toward the origin. To create this illustration, we have conducted optimizations over the entire constraint domain determined by $\widetilde{M}_{CO}/\widetilde{M}_{SCO}$ and $\widetilde{C}_{CO}/\widetilde{C}_{SCO}$. The colors in Fig. 10 indicate the number of layers of a material in the optimal solution obtained for a combination of constraints, regardless of the position of the constituent in the structure. As underlined in Section 6, the GA gradually incorporates aluminum and iron as the constraints become important. Aluminum is coupled to copper to achieve lower mass and iron is incorporated to reduce cost. The use of iron is restricted to the region below the cost constraint curve (red). Fig. 10 also provides the number of empty layers obtained in optimal designs. These results

[1] For interpretation of color in Figs. 8-10, the reader is referred to the web version of this article.

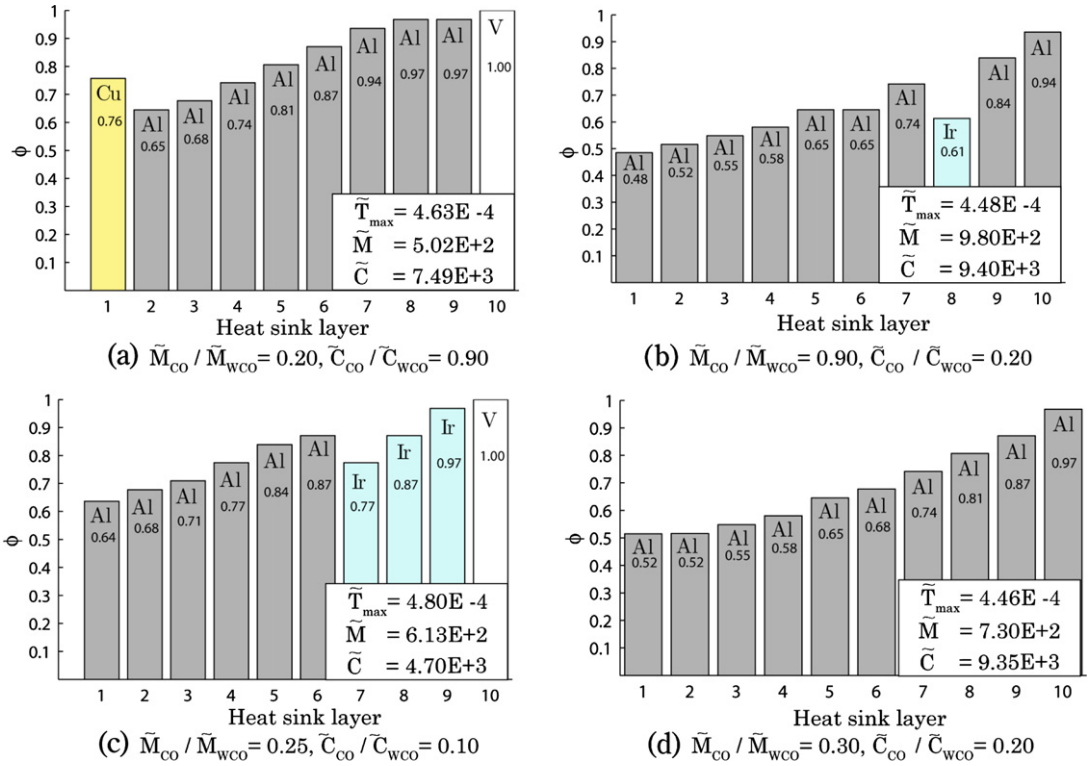

Fig. 9. Optimal designs under combinations of mass and cost constraints with $Ra\widetilde{D}^2 = 10^9$, $\widetilde{L} = 1$ and $N = 10$.

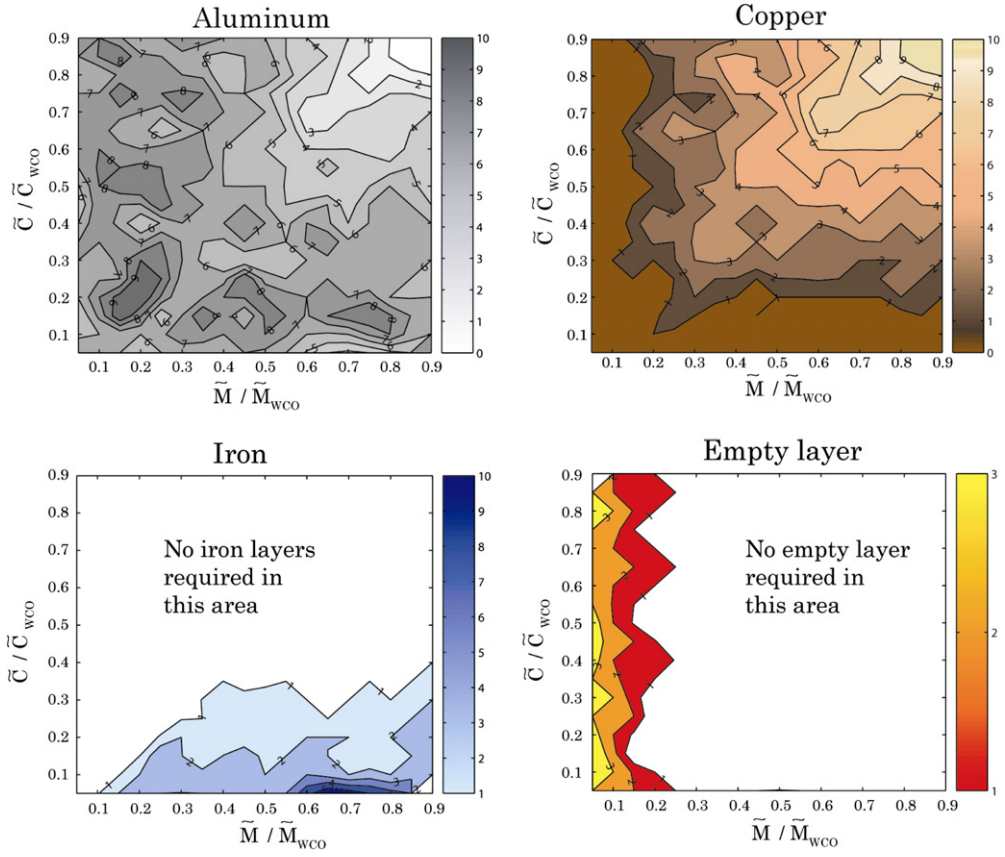

Fig. 10. Number of layers made of a specific material as a function of the combination of constraints for $Ra\widetilde{D}^2 = 10^9$, $\widetilde{L} = 1$ and $N = 10$.

indicate that the GA has adjusted the heat sink length to respect constraint. We note that this behavior is only present for stringent mass limitations. In sum, with the use of Fig. 10 one can rapidly determine which material to choose to build a heat sink that will fit his requirements.

10. Conclusions

In this paper, we minimized the hot spot $\widetilde{T}_{\max}$ of a heat sink made of a stacking of porous layers working in natural convection. Unconstrained as well as constrained designs have been presented. The considered constraints include the number of layers, the material in which each layer is made, as well as the porosity of the material. A combination of these constraints has also been considered. We determined optimal internal architecture by varying the porosity distribution and the material sequence. We also demonstrated that a large flexibility in the structure (design variables) permits to reach good thermal performances even in stringent environment. We found that under a combination of cost and mass constraints, the design domain is divided in three separate regions. Two curves delimit the mass and cost dominance. Both the mass and cost constraints are active for the optimal designs that fall between the two curves.

The present work allowed to determine optimal distribution of porosity and material composition of the system in the same manoeuvre. The optimization procedure by GA proved to be particularly efficient in the identification of a solution subjected to constraints. Our work has lead to families of designs that respond to a competition between hot spot temperature, size, mass, and cost requirements.

Future work could combine the results obtained in this paper with the ones presented in [23,24] for mixed convection problems. Based upon the optimal heat-generating plate density for mixed convection condition reported in [38], we expect that the optimal architecture will depend upon the imposed pressure drop (Bejan number) and the Rayleigh number. Furthermore, the flow regime (laminar vs. turbulent) could eventually be optimized rather than assumed [6,39].

Acknowledgement

This work was supported by the Natural Sciences and Engineering Research Council of Canada (NSERC).

References

[1] G.E. Moore, Cramming more components onto integrated circuits, Electronics 38 (8) (1965).
[2] J. Harvest, A.S. Fleischer, R.D. Weinstein, Modeling of the thermal effects of heat generating devices in close proximity on vertically oriented printed circuit boards for thermal management applications, Int. J. Therm. Sci. 46 (3) (2007) 253–261.
[3] A. McWilliams, The market for thermal management technologies, Business Communications Company, GB-SMC024D, 2006, p. 281.
[4] A.D. Kraus, A. Bar-Cohen, Thermal Analysis and Control of Electronic Equipment, McGraw-Hill, New York, 1983.
[5] A.K. da Silva, L. Gosselin, On the thermal performance of an internally finned three-dimensional cubic enclosure in natural convection, Int. J. Therm. Sci. 44 (6) (2005) 540–546.
[6] L. Gosselin, Fitting the flow regime in the internal structure of heat transfer systems, Int. Commun. Heat Mass Transfer 33 (1) (2006) 28–36.
[7] A.K. da Silva, A. Bejan, Constructal multi-scale structure for maximal heat transfer density in natural convection, Int. J. Heat Fluid Flow 26 (1) (2005) 34–44.
[8] T. Bello-Ochende, A. Bejan, Constructal multi-scale cylinders with natural convection, Int. J. Heat Mass Transfer 48 (21–22) (2005) 4300–4306.
[9] A. Bejan, Designed porous media: maximal heat transfer density at decreasing length scales, Int. J. Heat Mass Transfer 47 (14–16) (2004) 3073–3083.
[10] S. Hong, D.R. Herling, Open-cell aluminum foams filled with phase change materials as compact heat sinks, Scripta Mater. 55 (10) (2006) 887–890.
[11] T. Fend, R. Pitz-Paal, O. Reutter, J. Bauer, B. Hoffschmidt, Two novel high-porosity materials as volumetric receivers for concentrated solar radiation, Sol. Energy Mater. Sol. Cells 84 (2004) 291–304.
[12] Y.-T. Yang, C.-Z. Hwang, Calculation of turbulent flow and heat transfer in a porous-baffled channel, Int. J. Heat Mass Transfer 46 (5) (2003) 771–780.
[13] K. Boomsma, D. Poulikakos, F. Zwick, Metal foams as compact high performance heat exchanger, Mech. Mater. 35 (12) (2003) 1161–1176.
[14] G. Hetsroni, M. Gurevich, R. Rozenblit, Sintered porous medium heat sink for cooling of high-power mini-devices, Int. J. Heat Fluid Flow 27 (2) (2005) 259–266.
[15] Y.S. Muzychka, Constructal multi-scale design of compact microtube heat sinks as heat exchangers, Int. J. Therm. Sci. 46 (3) (2007) 245–252.
[16] X. Wei, Y. Joshi, Optimization study of stacked micro-channel sinks for micro-electronic cooling, IEEE Trans. Compon. Pack. Technol. 26 (1) (2003) 55–61.
[17] K. Jeevan, G.A. Quadir, K.N. Seetharamu, I.A. Azid, Z.A. Zainal, Optimization of thermal resistance of stacked micro-channel using genetic algorithms, Int. J. Numer. Methods Heat Fluid Flow 15 (1) (2005) 27–42.
[18] K. Foli, T. Okabe, M. Olhofer, Y. Jin, B. Sendhoff, Optimisation of micro heat exchanger: CFD, analytical approach and multi-objective evolutionary algorithms, Int. J. Heat Mass Transfer 49 (5–6) (2006) 1090–1099.
[19] P. Jiang, M. Fan, G. Si, Z. Ren, Thermal-hydraulic performance of small scale micro-channel and porous-media heat-exchangers, Int. J. Heat Mass Transfer 44 (5) (2001) 1039–1051.
[20] D.A. Nield, A. Bejan, Convection in Porous Media, second ed., Springer-Verlag, New York, 1992.
[21] M.A. Saada, S. Chikh, A. Campo, Natural convection around a horizontal solid cylinder wrapped with a layer of fibrous or porous material, Int. J. Heat Fluid Flow, doi:10.1016/j.ijheatfluidflow.2006.05.003.
[22] A. Bejan, Convection Heat Transfer, third ed., Wiley, 2004.
[23] P. Wildi-Tremblay, L. Gosselin, Layered porous media architecture for maximal cooling, Int. J. Heat Mass Transfer 50 (3–4) (2007) 464–478.
[24] G. Leblond, L. Gosselin, Effect of non-local equilibrium on minimal thermal resistance of porous layered systems, Int. J. Heat Fluid Flow 29 (1) (2008) 281–291.
[25] D.C. Pham, S. Torquato, Strong-contrast expansions for the effective conductivity of isotropic multiphase composites, J. Appl. Phys. 94 (10) (2003) 6591–6602.
[26] S.J. Kim, D. Kim, D.Y. Lee, On the local thermal equilibrium in microchannel heat sinks, Int. J. Heat Mass Transfer 43 (10) (2000) 1735–1748.

[27] O.M. Haddad, M.A. Al-Nimr, A.N. Al-Khateeb, Validity of the local thermal equilibrium assumption in natural convection from a vertical plate embedded in a porous medium, J. Porous Media 8 (1) (2005) 85–95.
[28] F.P. Incropera, D.P. DeWitt, Fundamentals of Heat and Mass Transfer, fifth ed., Wiley, 2002.
[29] http://www.metalprices.com (08/2006).
[30] J.H. Ferziger, Milovan Peric, Computational Methods for Fluid Dynamics, third ed., Springer, 2002.
[31] J.C. Tannehill, D.A. Anderson, R.H. Pletcher, Computational Fluid Mechanics and Heat Transfer, second ed., Taylors & Francis, 1997.
[32] C. Villemure, Optimization with genetic algorithms of a porous heat exchanger submitted to a constant heat flux in natural convection, Master's Dissertation, Université Laval, Québec City, Québec, Canada, 2007.
[33] http://www.zalmanusa.com (09/2006).
[34] Fluent User's Guide, 1998. <http://www.fluent.com>.
[35] A. Chipperfield, P. Fleming, H. Pohlheim, C. Fonseca, Genetic algorithm toolbox for use with Matlab, IEE Colloquium on Applied Control Techniques Using Matlab 14 (1995) 10/10-14.
[36] J. Chen, X. Yang, Optimal parameter estimation for Muskingum model based on gray-encoded genetic algorithm, Commun. Nonlinear Sci. Numer. Simul., 2005, doi:10.1016/j.cnsns.2005.06.005.
[37] F. Bobaru, S. Rachakonda, Optimal shape profiles for cooling fins of high and low conductivity, Int. J. Heat Mass Transfer 47 (23) (2004) 4953–4966.
[38] T. Bello-Ochende, A. Bejan, Optimal spacings for mixed convection, J. Heat Transfer – Trans. ASME 126 (6) (2004) 956–962.
[39] L. Gosselin, Minimum pumping power fluid tree networks without a priori flow regime assumption, Int. J. Heat Mass Transfer 48 (11) (2005) 2159–2171.